Transverse deformation of a lamellar TiAl alloy at high temperature by *in situ* microcompression

Thomas Edward James **Edwards**[a, 1] Corresponding author (teje2@cam.ac.uk)

Fabio **Di Gioacchino**[a] (fd302@cam.ac.uk)

Amy Jane **Goodfellow**[a] (ajg210@cam.ac.uk)

Gaurav **Mohanty**[b, c] (gaurav.mohanty@tut.fi)

Juri **Wehrs**[b] (juri.wehrs@empa.ch)

Johann **Michler**[b] (johann.michler@empa.ch)

William John **Clegg**[a] (wjc1000@cam.ac.uk)

[a]*Department of Materials Science and Metallurgy, 27 Charles Babbage Rd, University of Cambridge, Cambridge CB3 0FS, UK*

[b]*Empa, Swiss Federal Laboratories for Materials Science and Technology, Laboratory for Mechanics of Materials and Nanostructures, Feuerwerkerstrasse 39, 3602 Thun, Switzerland*

[c]*Laboratory of Materials Science, Tampere University of Technology, P.O. Box 589, 33101 Tampere, Finland*

Abstract (216 words)

The distribution of strain in hard mode oriented lamellar stacks of the two-phase γ-TiAl/α_2-Ti_3Al alloy Ti-45Al-2Nb-2Mn (at.%)-0.8 vol.% TiB_2 was measured at several temperatures up to 633 ºC by *in situ* micropillar compression, complemented by electron backscatter diffraction orientation mapping and digital image correlation strain mapping of a thermally stable surface Pt speckle pattern. Post-mortem

[1] Current address: Empa, Swiss Federal Laboratories for Materials Science and Technology, Laboratory for Mechanics of Materials and Nanostructures, Feuerwerkerstrasse 39, 3602 Thun, Switzerland

transmission electron microscopy further identified the finest scale deformation structures. It was found that slip and twinning transverse to the lamellae operates within discreet bands that zigzag across the lamellar structure. The shear strain within each band is approximately constant across the pillar width. This is inconsistent with current energetic models for transverse twin formation in γ-TiAl, which assume independent, non-interacting twins. This is explained using a mathematical formulation for the stress required to operate this transverse mechanical twinning as a function of strain. This study has elucidated how the multi-scale combination of several transverse twinning systems on different {111} planes in γ-TiAl lamellae can relieve the elastic stresses generated at a lamellar interface by the primary (highest Schmid factor) twinning system. It is thought that the facilitation of this mechanism will promote the ductilisation of lamellar γ-TiAl alloys. This is crucial for an increased damage tolerance and ease of component manufacture, leading to a more widespread use of γ-TiAl alloys.

Keywords: titanium aluminide polysynthetically twinned crystal (PST); deformation twinning; electron backscattering diffraction (EBSD); digital image correlation; scanning transmission electron microscopy;

1. Introduction

There is considerable recent interest [1-3] in the use of lamellar γ-TiAl alloys in high temperature turbine applications where the component has been grown as a bulk single, polysynthetically twinned (PST), crystal. The envisaged optimum is a lamellar orientation parallel to the blade axis, such that slip and twin systems operate primarily on the $\{111\}_\gamma$ planes transverse to the lamellae. This orientation allows for considerable Hall-Petch strengthening through interaction of the transverse systems with the lamellar interfaces, and also the avoidance of easy glide and twinning along the longitudinal deformation systems, operating parallel to the lamellar interfaces, which are now suppressed by the near-zero Schmid factor. $<11\bar{2}]\{111\}$ twin formation in γ-TiAl, when unconstrained, has been shown [4] to operate at resolved shear stresses lower than those required to activate the alternative $<1\bar{1}0]\{111\}$ ordinary or $<\bar{1}01]\{111\}$ super-dislocation slip systems at room temperature. Twinning is therefore a major mechanism in the deformation of lamellar γ-TiAl alloys.

The low ductility of polycrystalline γ-TiAl alloys, often below 0.02 plastic strain at room temperature [5], limits their damage tolerance and the ease of component manufacture. The early onset of crack formation may be associated with the local accumulation of elastic stresses at certain microstructural and plasticity features. Methods to characterise and model the development of such localised stresses during the operation of the above transverse deformation systems is therefore desirable to have predictive power over the mechanical performance of the proposed macroscopic components constituted of a single stack of γ-TiAl/α_2-Ti_3Al lamellae with planar interfaces parallel to the loading direction.

Energetic models exist for the formation of parallel-sided twins such as the fine transverse ones found in lamellar γ-TiAl alloys [6-8]; these models consider the energy cost of forming extra boundaries and of storing elastic energy in the surrounding lamellae, in exchange for the work done in passing twinning dislocations and hence generating a measureable strain. Transverse twins are thought to be nucleated from lamellar boundary misfit dislocations. The models assume independently developing transverse

twins consistent with observations of randomly located transverse twins observed in lamellar Ti-48Al-2Cr after tensile testing to a strain of 8.9 % at 800°C [9].

However, in other cases, the effect of surrounding plasticity results in new twins forming in locations dependent on those of transverse twins or slip in neighbouring lamellae, i.e. transverse strain transmission mechanisms. This is seen in Ti-48Al-0.37C compressed at room temperature to a strain of 3% [10], Ti-48Al-2Cr tensile tested at room temperature to 0.5 % strain [5] and Ti-45Al-2Nb-2Mn (at.%)-0.8 vol.% TiB_2 compressed to 3 % strain at 700 °C [11].

Recent microcompression testing [4, 12, 13] up to 700 °C on soft-mode oriented lamellar stacks (the angle, Φ, between lamellar planes and loading axis is $15° < \Phi < 75°$) of Ti-45Al-2Nb-2Mn (at.%)-0.8 vol.% identified the importance of the softening of constraint surrounding mechanical twins operating parallel to lamellae on the increasing ease for twinning with temperature. A mathematical formulation [4] of the physical condition for twinning was further developed to understand the dependence of the twinning onset stress on temperature, strain and strain rate. The use of microcompression specimens allows for the testing of single stacks of γ-TiAl/α_2-Ti_3Al lamellae in specific orientations, produced from complex, technologically-relevant alloy compositions that cannot be straightforwardly processed into macroscopic polysynthetically twinned crystals. In further microcompression studies [13], it has been shown that even upon just monotonic loading below the general polycrystal yield stress, such as at stresses that may be achieved in aerospace applications [14], certain lamellar colonies deform plastically. Further, the relative activity of deformation mechanisms, e.g. parallel or transverse to the lamellae, can be temperature dependent [11].

To better understand the spatial distribution of deformation operating on mechanisms transverse to the lamellar planes, and its dependence on test temperature, lamellar stacks of Ti-45Al-2Nb-2Mn (at.%)-0.8 vol.% with $\Phi < 15°$ were microcompressed *in situ* at several temperatures up to 633 °C. Strain localisation was mapped by digital image correlation of a thermally stable surface Pt speckle pattern, and

investigated further by transmission electron imaging. The results were then compared with two mathematical formulations for twinning in γ-TiAl developed elsewhere [4, 6].

2 Experimental Procedures

2.1 Material and metallographic preparation

Hard mode oriented cuboidal microcompression specimens 5 × 5 × 12 μm^3 in size, Fig. 1(a), were produced in single colonies of a commercial TiAl alloy of measured composition Ti-44.7Al-1.8Nb-1.8Mn (at.%)-0.8 vol.% TiB_2 (Ti4522XD) [15], and microstructural parameters given in Table 1, by Ga^+ focussed ion beam (FIB) milling in a scanning electron microscope (SEM) (Helios NanoLab, FEI, USA). The micropillars were located close to a sample edge, as described elsewhere [12]. The alloy condition is identical to that in [4]. At least two pillars were tested at each temperature: 25, 367 and 633 °C; the specimen number was limited by the complexity of the high temperature strain mapping method.

The crystal orientations of the lamellae and their angle to the loading axis, Φ, at the exposed side face of the pillars were determined before compression by electron backscatter diffraction (EBSD) (NordlysNano, Oxford Instruments, UK) on the FIB/SEM, similarly to [12]. EBSD data was analysed using the MTEX toolbox [16] for Matlab (Mathworks, UK).

2.2 Mechanical testing

Mechanical testing was undertaken using a 10 μm diamond flat punch (Synton, Switzerland) at temperatures up to 633 °C on a SEM nanoindenter (Alemnis, Switzerland) [17, 18]. Sample installation, *in situ* imaging and temperature tuning were performed identically to the procedure in [4].

The loading sequence for the micropillar compression tests in displacement control was a loading at 0.05 μm s^{-1} (strain rate of ~4 × 10^{-3} s^{-1}) to 1.2 μm (before rig compliance correction), followed by immediate unloading at the same rate. The unloading was paused at ~2 mN and the load drift rate was measured to ensure it was low. This rarely exceeded 10 μN s^{-1}.

2.3 Mapping of surface strain

Surface strain mapping of the exposed pillar side face was achieved by digital image correlation (DIC) of electron images of the Pt speckle pattern that was electron beam deposited following pre-test EBSD mapping, as in [12, 19]. DIC of pre- and post-deformation images was performed equivalently to [4, 12] with a subset size of 16 × 16 px^2, giving a resolution of 108 × 108 nm^2, using a 25% overlap. Correlation of the same unstressed region imaged before and after thermal exposure at 633 °C indicated an average noise level in the maximum shear strain measured per subset of 0.7 ± 0.4 %. Such noise levels were well suited to the identification of the shear strain of micro slip and twin bands. Comparison between EBSD maps acquired before and after compression enabled the identification of transverse mechanical twinning by an equivalent method to that reported in [12] for the identification of longitudinal mechanical twins. The rotation of the crystal lattice about the x, y and z-axes, θ_1, θ_2 and θ_3, relative to an arbitrary reference orientation was extracted using a method described elsewhere [19] after execution of the VarRe program in [11] to remove the known rotation offset between γ-TiAl variants resulting from their growth from a same parent α-TiAl grain according to the Blackburn relationship [20].

2.4 Transmission electron imaging of dislocation-twin structures

FIB thinned slices of pillars after compression, extracted from locations indicated in Fig. 1(a), were imaged in a 200 kV, field emission gun transmission electron microscope (FEG-TEM - Osiris, FEI, USA), operated in scanning mode (STEM) with both bright field (BF) and high angle annular dark field (HAADF) detectors. Before FIB extraction, the pillars were first protected with a coating of electron beam-deposited gas-injected Pt, followed by ion-beam deposited Pt.

3 Results

3.1 Crystal orientation and strain mapping

The loading curves for pillars compressed at 25 °C, 367 °C and 633 °C are given in Fig. 1(b); strain mapping datasets for the same pillars are given in Fig. 2. Lamellar interfaces were extracted from the pre-

compression crystal orientation maps, Fig. 2(d, i, n), and overlaid on the strain maps, Fig. 2(e, j, o). From the latter, the most striking observation is that the bands of shear operating transverse to the lamellae interfaces are clearly aligned from one lamella to the next as continuous zigzagging lines of high shear strain stretching the full width of the pillar. In Fig. 3(a,b), crystal orientation mapping of a zigzagging transverse band of shear before and after compression at 25 °C, as identified in the DIC strain map, Fig. 3(c), is able to identify coarse transverse twinning as the active deformation mechanism in a subset of the γ-TiAl lamellae. The remainder of the lamellae in Fig. 3(a) therefore deform by dislocation glide to generate the shear strain measured by DIC.

Though the shear strain of each of these 'transverse bands' varies along the height of the pillar from one band to the next, the shear strain within each band is relatively constant. That is to say that along a given transverse band, the extent of plastic (and retained elastic) shear strain is the same for all the differently oriented γ-TiAl lamellae present in the pillar. In fact, this uniformity of shear strain includes the α_2-Ti_3Al lamellae, which are observed to slip by a similar magnitude to the shear strain of the γ-TiAl lamellae, except for that the slip trace in α_2-Ti_3Al is now perpendicular to the pillar axis. Upon SEM imaging the pillar at an incline, Fig 2(c, h, m), the slip steps on the front and side of the pillar reveal both the {111} type slip or twin planes in γ-TiAl extending into the pillar depth, and the slip steps of the transverse bands as they propagate through the α_2-Ti_3Al lamellae. Recognising the Blackburn relationship between α_2-Ti_3Al and γ-TiAl [20], the horizontal slip trace orientation in α_2-Ti_3Al was indicative of prismatic slip occurring in the α_2-Ti_3Al lamellae loaded with $\Phi < 15°$.

Therefore, as far as the resolution of the image correlation strain maps can measure, across the temperature range studied on Ti4522XD, the development of transverse shear strain is morphologically identical.

To understand better the solid-state mechanics of the deformation occurring, attention was focussed on the pillar compressed at 633 °C where such extended 'transverse bands' were well defined. A variety of strain components were extracted from the DIC displacement field, Fig. 4, including the rotation of the

underlying crystal lattice, θ_3, per γ-variant, Fig. 4(e,f) according to a method described elsewhere [19]. From Fig. 4(b) it is apparent that the majority of the vertical compression of the pillar is achieved within the zigzagging transverse bands (ε_{yy} being greatest there). The rotation of the pillar in the plane of measurement, ω_3, in Fig. 4(c) indicates a region of high counter clockwise rotation (in excess of 9°) in the wide I_M lamella, stretching downwards from the top of the pillar, where friction against the punch surface imposes high lateral constraint. In Fig. 4(e), where the rotation of the I_M lattice is mapped, the same region corresponds to one of clockwise rotation (up to ~5°); this rotation of the crystal lattice opposes the rotation imposed by shear along the transverse bands in this lamella. However, besides this plume of heightened strain near the punch-pillar interface, no in-plane rotation of the underlying crystal lattice occurs elsewhere in the pillar, in either I_M or I_T lamellae, Fig. 4(e,f), within the noise of DIC measurement. This is perhaps surprising; several transverse bands of high shear strain operate in the mid-height region of the pillar (high ω_3), but at the DIC measurement scale no in-plane lattice rotation (low θ_3) compensates this shearing. Further mapping of the rotation of the crystal lattice of this pillar by EBSD mapping after compression yielded the projected rotation maps θ_1, θ_2 and θ_3, Fig. 5(a – c). The point-wise misorientation was measured relative to the arbitrary reference of the nominally constrained and unrotated region at the base of the pillar. In the map of θ_3, a macroscopic clockwise rotation of the central region of the pillar is measured; this mostly obscures any rotation related to the finer scale rotation feature at the top of the pillar. Nevertheless, there is a region of material differentially rotated in θ_1 relative to its surroundings, indicated in Fig. 5(a), in the location of the rotation feature measured by DIC. In addition, it is seen from the θ_1 and θ_3 components that a bending of the crystal lattice on the front face of the pillar occurs, as schematised in Fig. 5(d). The θ_2 component indicates that at the pillar surface there is no consistent twist along the pillar axis across all lamellae.

3.2 Transmission electron imaging

STEM imaging of a FIB lift-out from the centre of the pillar analysed in Fig. 4 and 5 was performed to characterise the deformation mechanisms associated with the zigzagging transverse bands and the apparent absence of lattice rotation to compensate high local single-system shearing. The positions of the

lamellar interfaces identified by pre-compression EBSD, Fig. 6(c), are easily identified on the BF and HAADF images of the pillar, Fig. 6(a,b). The transverse bands of shearing identified by DIC were found to correspond to the operation of relatively coarse transverse twins, and slip, depending on the γ-variant, where the twin thickness was *O*(100 nm). These coarse transverse bands of plasticity were found to align approximately across the lamellar interfaces, in agreement with the lower resolution DIC strain maps. This is detailed in Fig. 7; the indexing of $\{111\}_\gamma$ plane traces relates to Table 2, where the Schmid factors (S.F.s) for the various deformation mechanisms are given. This indicates that deformation II_T, for example, should operate entirely by dislocation motion, as all transverse twinning there either has a low S.F., or is Schmid forbidden.

In addition to the coarse transverse bands of plasticity, fine transverse nanotwins with a thickness *O*(10 nm) and operating on different $(111)_\gamma$ planes to the coarse bands (consistently that with the second highest S.F. for twinning) were observed to emit from the lamellar interfaces in regions of the pillar where the shear strain of transverse bands was highest. These are illustrated in the schematic in Fig. 7(f), where only a reduced amount of the fine twins in Fig. 7(d,e) are reproduced. Some of these fine twins traversed the full lamellar thickness, however most did not reach the midline of the lamella.

Elsewhere, STEM imaging of the top corners of the pillar slice, Fig. 8, indicated that the occurrence of such twinning on the secondary twinning system was intensive in such regions of complex multi-axial stress state arising from constraint by the punch [21]. Further, dislocation glide in the right-hand α_2-Ti_3Al lamella near the pillar-punch interface was similarly captured in Fig. 8(c,d). Along most of the length of the α_2 lamellae, there is little evidence of dislocation motion and the α_2 presumably only deforms elastically; however, in a few regions where transverse bands carry a higher shear strain, based upon DIC strain mapping, Fig. 4(a), strain transfer across the α_2 lamellae operates by slip, Fig. 9. This explains the handful of slip steps observed at the pillar surface along the α_2 lamellae in Fig. 2(b,c).

3.3 Boride particles in hard mode micropillars

Occasionally, EBSD mapping before compression revealed the existence of hard boride particles within the pillar volume. This is, for example, the case of the pillar reported in Fig. 10. From the corresponding loading curve, Fig. 1(b), this case is found to be much softer than boride-free pillars. Not only is the long boride flake seen to have cracked transversally, but it has also debonded from the lamellar TiAl matrix and sliding at this interface is also observed to have occurred. From this location, arrowed in the inset, Fig. 10(b), cracking extends into the γ-TiAl matrix.

4 Discussion

4.1 Accommodation of strain incompatibilities

It is encouraging for the meaningfulness of relating the DIC and the TEM results that the lamellar interfaces measured on the surface by EBSD map well onto the positions of interfaces imaged in the TEM slice from the middle of the pillar, such that the γ/α_2 structure is relatively invariant into the depth of the pillar here. Similarly, observations of slip steps in α_2-Ti_3Al lamellae on the surface of the pillar corroborate well with the dislocation structures observed in the same lamellae by TEM in the few locations where the local stress state imposed by transverse slip and twinning in the neighbouring γ-TiAl lamellae was sufficient to activate slip in the α_2, thereby ensuring some form of transverse strain transfer to the lamellae beyond.

Common disadvantages in the use of microcompression tests to evaluate bulk properties are size effects [22] and the absence of constraint at the free surfaces. In the current tests, both of these are avoided. In a previous study [23], it has been shown that for the presently used alloy, in the same lamellar orientation, pillar sizes above 3 μm width display a constant yield stress (pillars here are 5 μm wide). In short, above this threshold the lamellar thickness becomes the critical, dislocation nucleation-limiting wavelength, rather than the pillar size. Furthermore, the unconstrained, free surface effect here is expected to be minimal as the main constraint to transverse deformation is still the lamellar interfaces, of which there

are plenty in each pillar. This is the opposite case to soft-mode deformation of lamellar γ-TiAl, as investigated previously [4, 12], where the longitudinal twinning systems often are constrained neither by the boundaries in the lamellar structure, nor by the free surfaces of the micropillars.

The θ_1 rotation of the front surface of the pillar measured by EBSD is characteristic of two mechanisms – bulging or bending – elucidated by Daum *et al.* [24], and schematised in Fig. 5(d), which can occur in TiAl alloy samples compressed parallel to the lamellar orientation. The occurrence of bending was reported to be because of local buckling, and to therefore only onset beyond a buckling limit. As Daum *et al.* point out, deformation morphologies can be a combination of both individual modes, yielding apparent geometries such as axial twist. The extraction of the lamellar interfaces from the TEM images of the pillar mid-depth in Fig. 6(d) indicates symmetric distortion of the lamellar planes in the outwards direction, i.e. bulging.

The invariability of the deformation morphology for the temperatures studied for the hard-mode configuration contrasts with recent observations on the soft-mode lamellar orientation, whereby increasing temperature was found to favour longitudinal deformation mechanisms (operating parallel to the lamellar interfaces) over the transverse ones. It is possible that with the longitudinal deformation heavily repressed by a low Schmid factor in the current condition, the transverse mechanisms that dominate deformation in the hard-mode orientations generate equivalent deformation patterns on the DIC strain maps whether they are produced by slip or by twinning, such that a changing balance with temperature between the two mechanisms may not be fully captured by DIC. Nevertheless, the zigzagging morphology of strain transfer across lamellar interfaces remains at all temperatures.

It has previously been reported [12] that the resolution of EBSD mapping is generally too low to correctly identify most transverse twins in γ-TiAl, such that the TEM imaging is necessary to understanding the complete deformation mapped by DIC. Indeed, there were no indications on the DIC strain maps in Fig. 4(e,f) that a significant population of fine twins were operative on the secondary twin systems. This reflects the fact, remarked elsewhere [5], that despite there being numerous transverse

twins, their low thickness and relatively low shear strain means the contribution of such fine transverse twins to macroscopic strain may be very limited. Instead, the coarser transverse twinning and slip, with thicknesses *O*(100 nm), similar to those in [11, 25], operating on the systems with the highest Schmid factors, fulfil much of the macroscopic axial strain, according to the strain map in Fig. 4(b).

The observation by DIC strain mapping that the zigzagging bands of transverse deformation have a relatively constant shear strain from one side of the pillar to the other is compelling evidence of simultaneous and cooperative twin/slip band formation along each transverse band. Such uniformity of the magnitude of shear strain along extended transverse bands was similar for compressed Ti4522XD polycrystals [11]. In the least, twins that nucleate at higher strains must locate relative to pre-existent ones to develop the transverse bands observed here. One might think that this is driven by the potential to reduce elastic strain of the twinning shear at the twin ends. However, if one considers the schematic in Fig. 11 which presents a simplistic view of twinning as uniform blocks shearing, it is clear that twins (and eventually slip on sets of parallel planes, which results in a similar overall shape change [26]) within the zigzagging transverse bands operative in compression do not accommodate the elastic strain of each other's twinning shear, in fact they amplify it. This is because the lamellae are constrained to remain in contact with their neighbours, and the transverse twins are known to maintain parallel sides [10]. This concept was similarly seen for transverse twin propagation across a true twin interface in Ti-48Al-2Cr [27]; a high concentration of immobilised dislocations at the interface was observed, resulting in considerable lattice incompatibilities that were accommodated in a narrow region with a high defect density.

The question is therefore why the coarse transverse deformation bands are spatially correlated from one lamella to the next. In the case of true twin boundaries, as most are here, the propagation of transverse twins as a zigzagging *pilot* and *driven* pair has been reported by Singh *et al.* [28] on Ti-47Al-1Cr-0.2Si; similarly to here, in the pilot lamellae (presumably I_M from Schmid factor considerations, see Table 2) the highest S.F. between $<1\bar{1}0]\{111\}$ ordinary dislocation (O.D.) motion and $<11\bar{2}]\{111\}$ twinning was

for twinning. In the driven γ-variant, I_T here, twinning occurred in mirror symmetry to the pilot, about the interfacial plane, despite alternative deformation systems (only O.D. and twinning were considered, not superdislocation motion due to the considerably higher critical resolved shear stress for activation [29]) having higher S.F.s, therefore leading to Schmid law violation in I_T. It was proposed that [28] the incoming $1/6[11\bar{2}]_{I_M}$ Shockley twinning partial in I_M may dissociate at the interface to form a different $1/6<11\bar{2}]_{I_T}$ dislocation suitable for the operation of twinning in I_T, and an interfacial low-angle tilt boundary-type edge dislocation. This would proceed according to the double Thompson tetrahedron in Fig. 12(a) where ABC is the interfacial plane; using the notation in [30], the dislocation reaction occurs by the Burgers vector equation: **αB** = **α'B** + **αα'**. As **αB** dislocations arrive at the interface on successive BCD (i.e. $(\bar{a})$) planes, step 1 of Fig. 12(b), to operate twinning, they form a finite array of interfacial pilot dislocations that was determined [28] to impose a repulsive force on the driven **α'B** Shockley partial on BCD', (a'), planes, repelling **α'B** from the interface, step 2. Hereby, the operation of mirror symmetry twin transmission at a true twin interface may occur, driven by the possibility for a compressive axial strain to be generated by this twinning in both I_M and I_T, in the $\Phi \sim 0°$ orientation, despite the fact that it violates Frank's law [31], i.e. energy is put into the interface for the above dislocation dissociation reaction to occur.

At the interface, an array of sessile edge dislocations therefore develops [28], forming a low-angle tilt boundary. Based on the Thompson tetrahedron geometry, the residual interfacial dislocations **αα'** [32] have a Burgers vector type $2/9[111]$, and are oriented perpendicular to the interfacial plane; the line vector of these residuals must be along the intersection of the $(\bar{a})$ and (a') planes, i.e **BC**, such that the residual **αα'** is pure edge and lies on e.g. the $(1\bar{2}1)$ plane. It is possible that these recombine with further dislocations of the same nature to form perfect $1/3[111]$ ones which are known to densely populate γ/γ true twin interfaces [10, 33]. Such low angle tilt boundaries at γ/γ lamellar interfaces were previously measured in hard mode colonies of polycrystalline samples compressed at 700 °C [11]. On this premise

[28], the passage of twinning partial dislocations creates an increasing excess of vertical crystal planes towards the top of the twin configuration in Fig. 12(c), resulting in a region of compression at the interface at the top of the twins, and a tensile region at the bottom, respectively. This is essentially the same net stress distribution as proposed in Fig. 11(b). Therefore, although an axial strain is generated in both lamellae, the operation of the symmetrical, driven twin (or slip, which may similarly occur [28]) in I_T does not alleviate the strain incompatibilities of the pilot at the lamellar interface. Now, if deformation occurs on some of the alternative transverse $\{111\}_\gamma$ planes, it may be possible to relieve the elastic strain at the interface; this is illustrated in Fig. 11(c), where the operation of the fine nanotwins generates a shear strain (projected onto the plane of study) in the same sense as that of the impinging wide transverse bands in the neighbouring lamellae. In the notation above, other high energy interfacial edge dislocations **γγ'** on $\mathbf{(}\bar{2}11\mathbf{)}$ may dissociate according to **γγ'** = **γA** + **Aγ'**; this produces the **γA** dislocations to operate a secondary transverse twinning system in I_M by gliding on (c), as in Table 2 here, and **Aγ'** another secondary transverse twin in I_T by gliding on $\left(\bar{c}'\right)$. This dissociation reaction also violates Frank's rule and therefore requires an input of mechanical energy to operate. One may recognise that the Burgers vectors **αα'** = **γγ'** (also **αα'** = **ββ'**, but this case is redundant); however, the **αα'** $2/9\mathbf{[}111\mathbf{](}1\bar{2}1\mathbf{)}$ residual is sessile and pure edge, as is the **γγ'** $2/9\mathbf{[}111\mathbf{](}\bar{2}11\mathbf{)}$, such that **αα'** cannot re-orient its line vector by glide to cross-slip onto $\mathbf{(}\bar{2}11\mathbf{)}$ and become the necessary **γγ'** residual. Thermal activation of climb may permit this to operate along limited stretches to allow **αα'** = **γγ'** = **γA** + **Aγ'** to occur. Hence, the exact dislocation reactions that generate the secondary twinning systems are unconfirmed.

In short, it is found here that the operation of wide transverse twin and slip bands in $\Phi \sim 0°$ compression, which fulfil most of the axial strain of the pillar, is driven by the high Schmid factor of the pilot system, regardless of whether strain incompatibilities are generated at the interface. The additional operation of fine transverse twins on secondary systems in the near-interface region may provide some degree of accommodation of the strain incompatibilities caused by the wide transverse bands.

4.2 Implications for models of transverse twinning in lamellar γ-TiAl

Hence, from the results in the current work, and elsewhere [5, 8, 10, 11], it is not the case that transverse twins nucleate independently for all TiAl alloy compositions and mechanical test conditions. Indeed, there exists an effect of surrounding plasticity: new transverse twins or slip may form in locations dependent on those of transverse twins or slip in neighbouring lamellae. A comparable idea is also raised in the study of twin formation in an Mg alloy by Yu et al. [34], where experimental and modelling results indicated that the stress field of the twining dislocations at the twin tip could impede the nucleation of new twinning dislocations that would thicken the twin, such that the formation of many separate nano-twins could instead be favoured.

To better understand this in the γ-TiAl system consider the energetic model developed by Petryk *et al.* for transverse twinning of γ-TiAl. This model contains many similarities with a recent temperature dependent model for longitudinal twinning [4]. The twinning condition of Petryk *et al.* [8] for mechanical transverse twinning, in the notation of [4], is:

$$\tau_a{}^T = \tau_0 + \frac{\gamma_T}{h} + \tau_C \qquad (1)$$

where, $\tau_a{}^T$ is the resolved shear stress required to activate transverse twinning, γ_T the specific surface free-energy of the twin, h is an appropriate geometric (twin thickness) term for the parallel-sided plate twin geometry considered and τ_C is a dissipative stress term. The elastic resistance to the formation of parallel sided γ-TiAl transverse-type twins, τ_0, has been elegantly expressed as a function of the transverse twin geometry and related to experiment by Fischer *et al.* [6-8, 35].

With this expression for $\tau_a{}^T$ in mind, we look to the variational expressions in Appendix C of [4] for constrained longitudinal twinning. The extension to transverse twins is straightforward: the elastic term τ_0 and the extrinsic dissipative term (τ_C in [8], generalised to ξ in [4]) now refer mainly to processes occurring in the neighbouring lamellae to that undergoing transverse twinning, rather than the domains ahead of a longitudinal twin. Equivalent slip systems exist, albeit harder ones than in the longitudinal

case due to enhanced Hall Petch-type strengthening in the transverse direction. Otherwise, crystallographically, longitudinal and transverse twins are identical, both operating the $\langle 11\bar{2}]\{111\}$ system. We now consider the variation with strain at constant temperature and strain rate of the twinning condition in [4] to better understand the differential twin morphologies observable with transverse twins:

$$\left(\frac{\partial \tau_a{}^T}{\partial \varepsilon}\right)_{T,\dot{\epsilon}} = \frac{\Theta}{\Omega}\left(\frac{\partial \tau_0}{\partial \varepsilon}\right)_{T,\dot{\epsilon}} + \frac{\beta}{\Omega}\left(\frac{\partial \gamma_F}{\partial \varepsilon}\right)_{T,\dot{\epsilon}} + \frac{Z}{\Omega}\left(\frac{\partial \tau_y}{\partial \varepsilon}\right)_{T,\dot{\epsilon}} + \frac{\Psi}{\Omega}\left(\frac{\partial \tau_D{}^T}{\partial \varepsilon}\right)_{T,\dot{\epsilon}} \quad (2)$$

where β, Θ, Z, Ψ and Ω are positive as defined in [4], τ_y is the shear stress to activate extrinsic dislocation motion (i.e. other than the Shockley twinning partials), γ_F is the twinning shear fault energy and $\tau_D{}^T$ is the stress to activate the twin-mediating Shockley partial dislocations. Finally, T, ε and $\dot{\varepsilon}$ are the temperature, strain and strain rate, respectively. At lower, technologically relevant, strain levels, e.g. < 5 %, plasticity by dislocation glide in $\Phi \sim 0°$ pillars was not the dominant mechanism in γ-TiAl, rather transverse twinning abounded [8]. This means that extrinsic slip mechanisms (e.g. accommodative slip in the neighbouring lamellae, ahead of the transverse twins) are not particularly active, however the intrinsic ones, which mediate twinning (the Shockley twinning partials), must remain to progress the formation of transverse twins. Furthermore, as extrinsic slip mechanisms are initially absent and the Shockley twinning partials all travel in the same direction in the advancing plane of the twin, one may reasonably assume the increase in CRSS with strain of the Shockley partials to be initially minimal as locks are avoided. Hence, in this low strain range, the strain dependence of the stress to activate extrinsic dislocation motion, $\left(\partial \tau_y / \partial \varepsilon\right)_{T,\dot{\epsilon}}$, and that of the stress to activate twin-mediating dislocations, $\left(\partial \tau_D{}^T / \partial \varepsilon\right)_{T,\dot{\epsilon}}$, are null. In addition, the twinning shear fault energy, γ_F, is not expected to vary with strain level. Therefore:

$$\left(\frac{\partial \tau_a{}^T}{\partial \varepsilon}\right)_{T,\dot{\epsilon}} = \frac{\Theta}{\Omega}\left(\frac{\partial \tau_0}{\partial \varepsilon}\right)_{T,\dot{\epsilon}} \quad (3)$$

Eq. (3) is critical to the understanding of transverse twin morphologies. Indeed, whilst the elastic energy stored in neighbouring lamellae may increase with twin thickness as in [6], as straining progresses τ_0 may

decrease when viewed from the point of view of the formation of a transverse twin in the neighbouring lamellae with a shear that provides accommodation for the incompatibilities of a former. This would result from a reduced elastic impact of the new twin on its surroundings motivated by an easing of elastic stresses already present from transverse twins. In short, the shear strain of a second transverse twin may relax elastic strains generated by the shear of a first so that the $(\partial\tau_0/\partial\varepsilon)_{T,\dot{\epsilon}}$ term would be negative, as would $\left(\partial{\tau_a}^T/\partial\varepsilon\right)_{T,\dot{\epsilon}}$. This is presumably the case for the fine twins identified in the present study. Similarly, in reverse, a driven mirror twin nucleated in a given I_T lamella adjacent to the pilot twin in I_M, would therefore experience a higher elastic resistance to its growth than an isolated transverse twin.

Several groups have studied the mechanisms by which transverse twins nucleate in γ-TiAl [10, 36-38]. At γ/γ interfaces where a rotational misfit exists as a result of the tetragonality of the γ-TiAl phase, twins may nucleate from the $1/2<11\bar{2}]$ parallel screw dislocations that accommodate the twist misfit of the lattice across the interface [39]. The $1/3[111]$ edge dislocations evoked here that generate low angle tilt boundaries at true twin γ/γ interfaces are similarly reported to nucleate transverse twins in γ-TiAl [10, 33]; the population density of such interfacial dislocations depends on the processing route and the alloy composition. The apparent widespread existence of twin nucleation sites within the lamellar interfaces was certainly a motivation for the energy-based models [6-8] of isolated transverse twins; however, it has been demonstrated here that, based on dislocation reaction sequences investigated previously [28], the nucleation of a significant proportion of transverse twins in lamellar γ-TiAl depends on the existence of a *pilot* [28] twin system. Such twins would generate an elastic strain field that could either increase or decrease the elastic energy storage cost of forming a driven twin in the neighbouring lamella. In some cases, as the fine secondary twins here, this means that new transverse twins are nucleated adjacent to similarly shearing twins in the neighbouring lamella, where ${\tau_a}^T$ is lowest for the secondary fine twin, rather than elsewhere along the lamellar interface.

The above energetic models for transverse twinning [6-8] may hence only be applied to alloy conditions and test temperatures where twin formation to relieve neighbouring mechanical twins' elastic stress

fields, or otherwise, as a result of the existence of a pilot twin, is not dominant. This may be, for example, in a lamella that is not in contact with its true twin counterpart, i.e. it is bordered by order-variant and pseudo-twin γ/γ interfaces, or γ/α_2 interfaces, such that mirror symmetry twin propagation cannot occur to produce the zigzagging bands of transverse deformation seen here in the pillar compressed at 633 °C, Fig. 4. In the cases where twin formation is not independent of pre-existing twins, the models could only apply to the very first, considerably distant, pilot transverse twins formed, as these are necessarily independent.

Finally, one should consider the morphology of the parallel sets of zigzagging transverse bands that propagate over seven neighbouring I_M & I_T lamellae, as well as a few α_2 lamellae and other γ orientation variants in Fig. 2(d,e). All the I_M lamellae presumably experience a similar stress state, at least at the pillar mid-height, such than pilot twin systems may initiate in any of them. However, the coarse width slip and twin bands are not located haphazardly from one I_M/I_T true twin pair of lamellae to the next: they are organised into complete, and approximately equally spaced bands that stretch the full pillar width. This undoubtedly requires a considerably more simultaneous and cooperative growth process of twinning and slip per zigzagging transverse band than envisaged in the current models for transverse twinning.

4.3 Hard boride particles resulting in a softening of hard mode colonies

In physical metallurgy, a common result of the addition of hard particles to an alloy matrix is an increase in strength [40]. This occurs by forest hardening near the hard particles and an accumulation of geometrically necessary dislocations (GNDs) to uptake curvature of the matrix lattice surrounding the hard particles [41]. In the current hard mode oriented lamellar TiAl testpieces, however, hard particle addition can have a softening effect. Indeed, unlike approximately needle or spherical boride shapes seen in other TiAl alloys [42, 43], the flaky borides found in Ti4522XD constitute two-dimensional planes that, in many cases, extend the full colony width. The weak particle-matrix interface is easily debonded [15] such that the lamellar TiAl matrix can slide on the flaky borides for relatively long distances at a

lower stress than that required to activate transverse mode deformation mechanisms in the hard mode matrix.

5 Conclusions

In situ microcompression up to 633 °C of hard-mode oriented lamellar stacks (Φ < 15°) milled from single colonies of lamellar Ti-45Al-2Nb-2Mn (at.%)-0.8 vol.% TiB_2, complemented by a combination of EBSD crystal orientation mapping and digital image correlation strain mapping, demonstrated that the transverse shear generated by micro-slip and deformation twinning at all temperatures was found to align into transverse, zigzagging bands across the pillar width. Such zigzagging bands consisted of approximately uniform shearing in all γ-TiAl and α_2-Ti_3Al lamellae.

Further TEM imaging identified the zigzagging bands to result from mirror symmetry deformation mechanisms operating across true twin γ/γ interfaces, despite their strain being incompatible; further arrays of more refined twins (*O*(10 nm) thickness) provided some degree of accommodation to the high interfacial elastic strain generated by the coarse transverse deformation bands.

Such apparent cooperative, or at least elastic strain history-dependent, shearing contradicts the premise of current energetic models for transverse twin formation in γ-TiAl, which assume independently located and growing twins.

The present study has elucidated how the multi-scale combination of several transverse twinning systems on different {111} planes in γ-TiAl lamellae can relieve the elastic stresses generated at a lamellar interface by the primary (highest Schmid factor) twinning system. It is thought that the facilitation of this mechanism, by targeted alloying and processing to modify the lamellar interface structure and encourage nano-twin nucleation, will promote the ductilisation of hard-mode oriented bulk PST crystal γ-TiAl alloys, and more generally polycrystalline γ-TiAl alloys where such lamellar orientations also exist. This

is crucial for an increased damage tolerance and ease of component manufacture, leading to a more widespread use of γ-TiAl alloys.

Acknowledgements

The work was supported by the EPSRC / Rolls-Royce Strategic Partnership (EP/M005607/1). T.E.J.E. also acknowledges the kind support of the Worshipful Company of Armourers and Brasiers' Gauntlet Trust.

6 References

[1] G. Chen, Y. Peng, G. Zheng, Z. Qi, M. Wang, H. Yu, C. Dong, C.T. Liu, Polysynthetic twinned TiAl single crystals for high-temperature applications, Nat Mater 15(8) (2016) 876-881.

[2] M. Schutze, High-temperature alloys: single-crystal performance boost, Nat Mater 15(8) (2016) 823-824.

[3] T.E.J. Edwards, Recent progress in the high-cycle fatigue behaviour of γ-TiAl alloys, Materials Science and Technology (2018) 1-21.

[4] T.E.J. Edwards, F. Di Gioacchino, G. Mohanty, J. Wehrs, J. Michler, W.J. Clegg, Longitudinal twinning in a TiAl alloy at high temperature by in situ microcompression, Acta Materialia 148 (2018) 202-215.

[5] F. Appel, J.D.H. Paul, M. Oehring, Gamma titanium aluminide alloys : science and technology, Wiley-VCH, Weinheim, 2011.

[6] H. Petryk, F.D. Fischer, W. Marketz, H. Clemens, F. Appel, An energy approach to the formation of twins in TiAl, Metall and Mat Trans A 34(12) (2003) 2827-2836.

[7] F.D. Fischer, F. Appel, H. Clemens, A thermodynamical model for the nucleation of mechanical twins in TiAl, Acta Materialia 51(5) (2003) 1249-1260.

[8] M. Rester, F.D. Fischer, C. Kirchlechner, T. Schmoelzer, H. Clemens, G. Dehm, Deformation mechanisms in micron-sized PST TiAl compression samples: Experiment and model, Acta Materialia 59(9) (2011) 3410-3421.

[9] F. Appel, R. Wagner, M. Yoo, M. Wuttig, Twinning in advanced materials, TMS Symp. Proc., MH Yoo and M. Wuttig, eds., Warrendale, PA, 1994, pp. 317-30.

[10] F. Appel, An electron microscope study of mechanical twinning and fracture in TiAl alloys, Philosophical Magazine 85(2-3) (2005) 205-231.

[11] T.E.J. Edwards, F. Di Gioacchino, W.J. Clegg, An experimental study of polycrystalline plasticity in lamellar titanium aluminide, International Journal of Plasticity, submitted (2018).

[12] T.E.J. Edwards, F. Di Gioacchino, R. Muñoz-Moreno, W.J. Clegg, Deformation of lamellar TiAl alloys by longitudinal twinning, Scripta Materialia 118 (2016) 46-50.

[13] T.E.J. Edwards, F. Di Gioacchino, A.J. Goodfellow, G. Mohanty, J. Wehrs, J. Michler, W.J. Clegg, Deformation of lamellar γ-TiAl below the general yield stress, Acta Materialia 163 (2019) 122-139.

[14] D. Rugg, M. Dixon, J. Burrows, High-temperature application of titanium alloys in gas turbines. Material life cycle opportunities and threats – an industrial perspective, Materials at High Temperatures 33(4-5) (2016) 536-541.

[15] T.E.J. Edwards, F. Di Gioacchino, R. Muñoz-Moreno, W.J. Clegg, The interaction of borides and longitudinal twinning in polycrystalline TiAl alloys, Acta Materialia 140(Supplement C) (2017) 305-316.

[16] F. Bachmann, R. Hielscher, H. Schaeben, Texture analysis with MTEX–free and open source software toolbox, Solid State Phenomena, Trans Tech Publ, 2010, pp. 63-68.

[17] J.M. Wheeler, P. Brodard, J. Michler, Elevated temperature, in situ indentation with calibrated contact temperatures, Philosophical Magazine 92(25-27) (2012) 3128-3141.

[18] J.M. Wheeler, J. Michler, Elevated temperature, nano-mechanical testing in situ in the scanning electron microscope, Review of Scientific Instruments 84(4) (2013) 045103.

[19] F. Di Gioacchino, W.J. Clegg, Mapping deformation in small-scale testing, Acta Materialia 78 (2014) 103-113.

[20] M.J. Blackburn, Trans. Metall. Soc. AIME 239 (1967) 1200.

[21] P.A. Shade, R. Wheeler, Y.S. Choi, M.D. Uchic, D.M. Dimiduk, H.L. Fraser, A combined experimental and simulation study to examine lateral constraint effects on microcompression of single-slip oriented single crystals, Acta Materialia 57(15) (2009) 4580-4587.

[22] S. Korte, W.J. Clegg, Discussion of the dependence of the effect of size on the yield stress in hard materials studied by microcompression of MgO, Philosophical Magazine 91(7-9) (2010) 1150-1162.

[23] A.J. Palomares-García, M.T. Pérez-Prado, J.M. Molina-Aldareguia, Effect of lamellar orientation on the strength and operating deformation mechanisms of fully lamellar TiAl alloys determined by micropillar compression, Acta Materialia 123 (2017) 102-114.

[24] B. Daum, G. Dehm, H. Clemens, M. Rester, F.D. Fischer, F.G. Rammerstorfer, Elastoplastic buckling as source of misinterpretation of micropillar tests, Acta Materialia 61(13) (2013) 4996-5007.

[25] F. Appel, U. Christoph, Coherency stresses and interface-related deformation phenomena in two-phase titanium aluminides, Intermetallics 7(10) (1999) 1173-1182.

[26] F. Di Gioacchino, J. Quinta da Fonseca, An experimental study of the polycrystalline plasticity of austenitic stainless steel, International Journal of Plasticity 74 (2015) 92-109.

[27] F. Appel, P.A. Beaven, R. Wagner, Deformation processes related to interfacial boundaries in two-phase γ-titanium aluminides, Acta Metallurgica et Materialia 41(6) (1993) 1721-1732.

[28] J.B. Singh, G. Molénat, M. Sundararaman, S. Banerjee, G. Saada, P. Veyssière, A. Couret, The activation and the spreading of deformation in a fully lamellar Ti–47at.% Al–1at.% Cr–0.2at.% Si Alloy, Philosophical Magazine 86(16) (2006) 2429-2450.

[29] K. Fujimura, K. Kishida, K. Tanaka, H. Inui, Compression of micropillars of TiAl coexisting with Ti3Al, MRS Online Proceedings Library 1295 (2011) 201-206.

[30] N. Thompson, Dislocation nodes in face-centred cubic lattices, Proceedings of the Physical Society. Section B 66(6) (1953) 481.

[31] F.C. Frank, On the equations of motion of crystal dislocations, Proceedings of the Physical Society. Section A 62(2) (1949) 131.

[32] J.P. Hirth, J. Lothe, Theory of dislocations, (1982).

[33] F. Appel, R. Wagner, Microstructure and deformation of two-phase γ-titanium aluminides, Materials Science and Engineering: R: Reports 22(5) (1998) 187-268.

[34] Q. Yu, L. Qi, K. Chen, R.K. Mishra, J. Li, A.M. Minor, The nanostructured origin of deformation twinning, Nano Letters 12(2) (2012) 887-892.

[35] F. Appel, F.D. Fischer, H. Clemens, Precipitation twinning, Acta Materialia 55(14) (2007) 4915-4923.

[36] M.H. Yoo, Twinning and mechanical behavior of titanium aluminides and other intermetallics, Intermetallics 6(7) (1998) 597-602.

[37] Z. Jin, T.R. Bieler, An in-situ observation of mechanical twin nucleation and propagation in TiAl, Philosophical Magazine A 71(5) (1995) 925-947.

[38] S. Farenc, A. Coujou, A. Couret, An in situ study of twin propagation in TiAl, Philosophical Magazine A 67(1) (1993) 127-142.

[39] B.K. Kad, P.M. Hazzledine, Shear boundaries in lamellar TiAl, Philosophical Magazine Letters 66(3) (1992) 133-139.

[40] A. Kelly, R.B. Nicholson, Precipitation hardening, Progress in Materials Science 10(Supplement C) (1963) 151-391.

[41] P.S. Karamched, A.J. Wilkinson, High resolution electron back-scatter diffraction analysis of thermally and mechanically induced strains near carbide inclusions in a superalloy, Acta Materialia 59(1) (2011) 263-272.

[42] D. Hu, Role of boron in TiAl alloy development: a review, Rare Metals 35(1) (2015) 1-14.

[43] Y.H. Wang, J.P. Lin, Y.H. He, Y.L. Wang, G.L. Chen, Microstructural characteristics of Ti–45Al–8.5Nb/TiB2 composites by powder metallurgy, Journal of Alloys and Compounds 468(1-2) (2009) 505-511.

Figure Captions

Figure 1 (a) schematic of a micropillar specimen milled from a lamellar two-phase titanium aluminide alloy in the hard mode orientation ($\Phi < 15°$), with the location of TEM foil lift-out dotted in black. (b) loading curves for the hard-mode pillars compressed at 25 °C, 367 °C and 633 °C in Fig. 2. In (b) the curve in blue corresponds to the pillar in Fig. 10 where a TiB_2 particle is present, causing plasticity to onset at a lower stress level than the boride-free pillars. Experimental issues unfortunately meant that the acquisition of the stress-strain data for the pillar compressed at 633 °C (green) was interrupted early in the compression procedure; the maximum strain applied is known nonetheless.

Figure 2 Deformation mapping of hard mode pillars compressed at 25, 367 and 633 °C. The pre- and post-compression electron images (a,b,f,g,k,l) are correlated to produce the strain maps (e,j,o) onto which are overlaid in white the lamellar interfaces extracted from the pre-compression EBSD maps (d,i,n). The EBSD colour code for the γ-TiAl lamellar structure is the same as used elsewhere [12]. The zigzagging bands of transverse plastic strain are arrowed in black in (e,j,o); such transverse deformation produces the surface slip lines arrowed on the side faces of the pillars in the details of the incline SE images (c,h,m). Prismatic slip lines of a α_2-Ti_3Al lamella are arrowed in black in (b) and white in (e).

Figure 3 Pre- (a) and post-test (b) EBSD maps of the mid-section of a pillar compressed at 25 °C, displaying transverse twins, as verified by a method in [12]; the EBSD colour scheme is the same as in Fig. 2. In (c) the DIC strain map of the same region is given, indicating that strain concentrates at the transverse twins. As reported previously, [12], deterioration of the Pt speckle pattern occurs above twinned regions, disrupting the DIC results, as arrowed in white. The black arrow indicates where transverse slip occurs.

Figure 4 Further components of strain extracted from the DIC maps data in Fig. 2(e). ω_3 is the curl of the displacement field about the axis perpendicular to the surface of measurement; θ_3 describes the rotation of the underlying crystal lattice per γ-variant, and is extracted following a method outlined in [19].

Figure 5 (a – c) rotation components θ_1, θ_2 and θ_3 of the γ-TiAl phase crystal lattice relative to the base of the pillar, extracted from the pre- and post-compression EBSD maps of the front face of the pillar compressed at 633 °C in Fig. 2. The effectiveness of the VarRe program is verified by application to the pre-compression state: all lamellae display θ_1, θ_2 and θ_3 values of zero, within the ~0.5° error of EBSD mapping. Note the different scales used for each rotation component. (d) schematic of the bulging and bending morphologies consistent with the crystal rotation of the front surface of the pillar.

Figure 6 STEM BF (b) and HAADF (c) images of thin foil lift-out of the pillar compressed at 633 °C in Fig. 2, along with the pre-compression EBSD map of the pillar surface for comparison of the lamellar boundary structure into the pillar depth. (d) positions of the lamellar interfaces, extracted from (b), illustrating the lateral bulging of the upper region

of the pillar; the dotted straight lines have been added as a guide to the eye. The STEM images were not taken normal to sample surface in order to increase the contrast on the deformation features; hence, lamellar boundaries appear to have a finite width in all the STEM images in the current work.

Figure 7 STEM BF (a,d) and HAADF (b,e) images of two regions indicated in Fig. 6 where plasticity occurs in mirror-symmetry coarse transverse bands in γ-TiAl lamellae. The drawings of the deformation structures (c,f) have been extracted from the STEM images; not all the fine nanotwins in (d,e) were reproduced in (f), for clarity.

Figure 8 STEM BF (a,c) and HAADF (b,d) images of two regions at the top of the pillar, indicated in Fig. 6, where a dense array of fine twins, of which a few are arrowed in black, were observed to operate in γ-TiAl lamellae on the secondary twinning systems, and dislocation glide mediates plasticity in α_2 lamellae.

Figure 9 STEM BF (a,c) and HAADF (b,d) images of two regions from the mid-height of the pillar indicated in Fig. 6 where transmission of transverse strain across α_2 lamellae occurs in some cases by dislocation glide (arrowed in red). Green arrows indicate relatively dislocation-free propagation of transverse shear across an α_2 lamella.

Figure 10 Secondary electron images before (a) and after (b – d) compression at 633 °C of a hard mode micropillar containing a TiB_2 flake, outlined in white in (a), that is seen to crack transversally and to debond from the γ-TiAl lamellar matrix; this resulted in a significantly lower yield stress for the onset of plasticity in Fig. 1(b) than in the absence of such boride particles. Transversal cracking of boride also extends into the γ-TiAl matrix, as arrowed in black in (b).

Figure 11 Schematic of the transverse twinning morphologies and strain accommodation mechanisms active upon mirror symmetry transverse twinning across true twin γ/γ interfaces.

Figure 12 (a) double Thompson tetrahedron describing the $\{111\}_\gamma$ planes across a true twin γ/γ interface according to the original notation established in [30]. The bold lines indicate ordinary dislocation $<1\bar{1}0]$ directions; the rest of the tetrahadral edges are $<10\bar{1}]$ superdislocations. Greek letters indicate the centroids of triangular faces opposite the corresponding capital roman lettered vertice. The dislocation decomposition in (b) converts an incoming Shockley partial $<11\bar{2}]$ twinning dislocation into a twinning partial on the mirror-symmetry transverse twinning plane and leaves a residual low-angle tilt boundary edge dislocation at the lamellar interface, which results in the elastic stress gradient along the interface depicted in (c).

Table 1 Microstructural dimensions of the Ti-45Al-2Nb-2Mn(at%)-0.8vol% TiB_2 (Ti4522XD) alloy, obtained from BSE images (colony size) and EBSD maps (lamellar dimensions).

Colony size /μm	α_2 fraction	Mean γ lamellar thickness /μm	Mean α_2 lamellar thickness /μm	Mean γ domain length /μm
70	9.5 %	1.4 ± 0.9	0.26 ± 0.09	9.7

Table 2 Schmid factors for the transverse twinning and dislocation glide mechanisms for the γ-TiAl variants present in the pillar tested at 633 °C in Fig. 4. The S.F. values were determined from the crystal orientations measured by EBSD before compression; the angular error of EBSD indexing resulted in some minor discrepancies in the third significant figure of the S.F. values between γ-variants of the same matrix/twin designation. The S.F.s of the coarse transverse twin systems for I_M and I_T are in bold; active secondary, fine nano-twin systems for the same γ-variants are in italics.

γ-variant	plane	twinning	conventional slip	
		$<11\bar{2}]$	$<1\bar{1}0]$ ordinary	$<10\bar{1}]$ super- (highest S.F.)
I_M	**(111)**	**0.355_C**	0.352	0.483
	$(\bar{1}11)$	*0.333_C*	0.245	0.411
	$(11\bar{1})$	0.203_C	0.124	0.238
I_T	**(111)**	0.165_C	0.127	0.206
	$(\bar{1}\bar{1}1)$	*0.252_C*	0.252	0.345
	$(1\bar{1}\bar{1})$	**0.303_C**	**0.393**	0.459
II_T	**(111)**	0.188_T	0.076	0.200
	$(\bar{1}11)$	0.195_C	**0.455**	0.396
	$(11\bar{1})$	0.099_C	0.338	0.255

Figure(s)

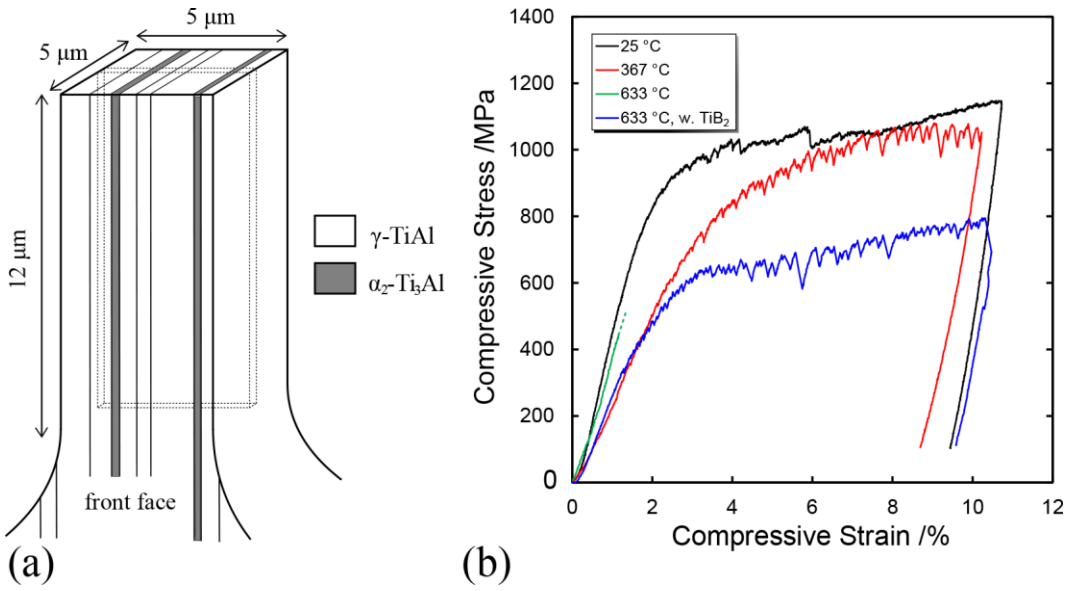

Figure 1 (a) schematic of a micropillar specimen milled from a lamellar two-phase titanium aluminide alloy in the hard mode orientation (Φ < 15°), with the location of TEM foil lift-out dotted in black. (b) loading curves for the hard-mode pillars compressed at 25 °C, 367 °C and 633 °C in Fig. 2. In (b) the curve in blue corresponds to the pillar in Fig. 10 where a TiB_2 particle is present, causing plasticity to onset at a lower stress level than the boride-free pillars. Experimental issues unfortunately meant that the acquisition of the stress-strain data for the pillar compressed at 633 °C (green) was interrupted early in the compression procedure; the maximum strain applied is known nonetheless.

Figure(s)

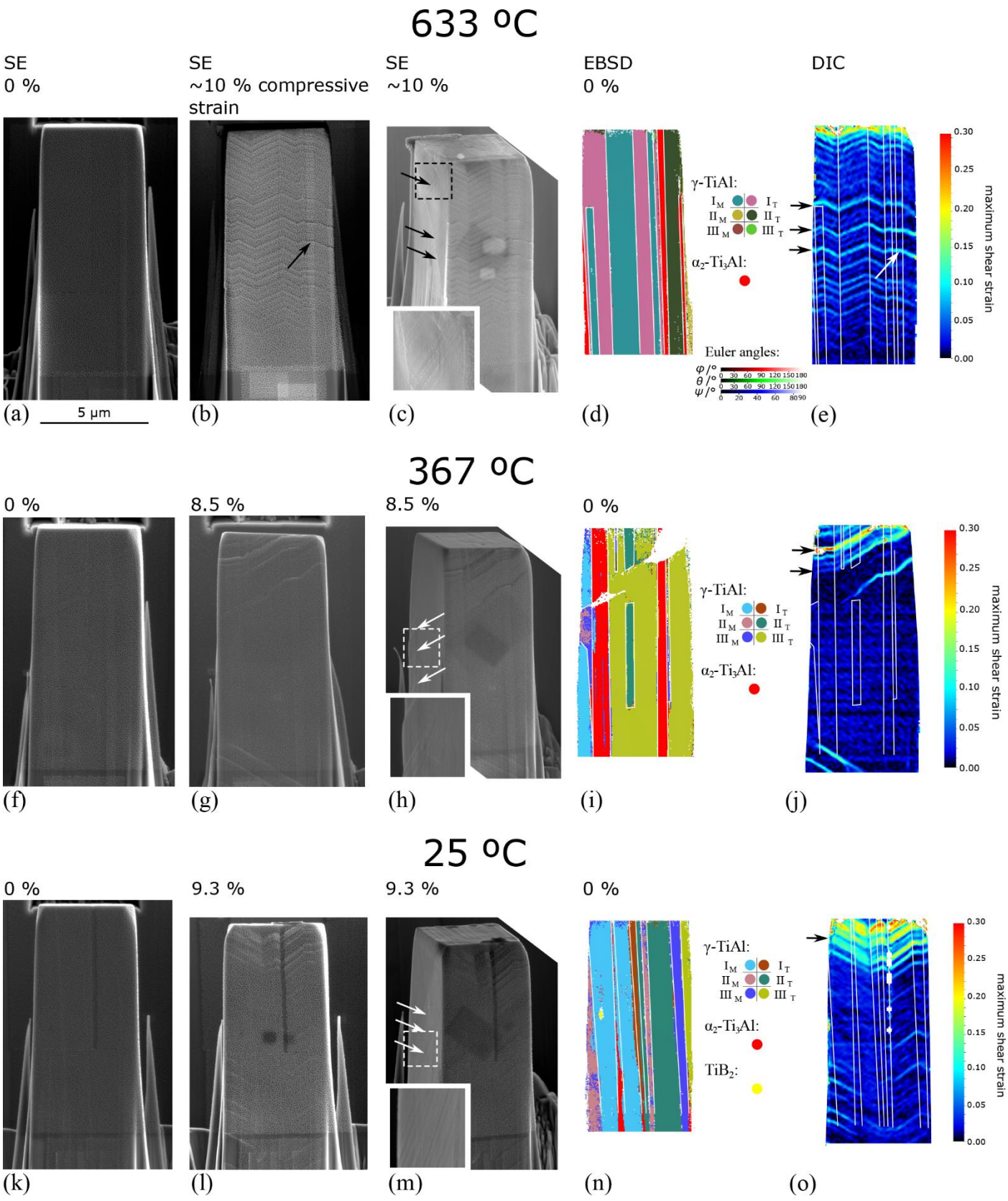

Figure 2 Deformation mapping of hard mode pillars compressed at 25, 367 and 633 °C. The pre- and post-compression electron images (a,b,f,g,k,l) are correlated to produce the strain maps (e,j,o) onto which are overlaid in white the lamellar interfaces extracted from the pre-compression EBSD maps (d,i,n). The EBSD colour code for the γ-TiAl lamellar structure is the same as used elsewhere [10]. The zigzagging bands of transverse plastic strain are arrowed in black in (e,j,o); such transverse deformation produces the surface slip lines arrowed on the side faces of the pillars in the incline SE images (c,h,m). Prismatic slip lines of a α_2-Ti_3Al lamella are arrowed in black in (b) and white in (e).

Figure(s)

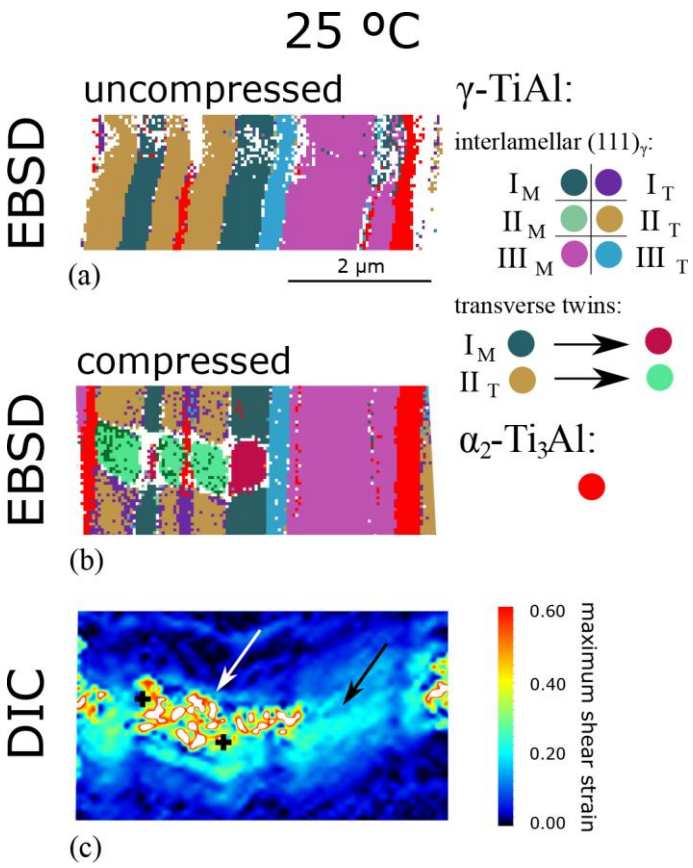

Figure 3 Pre- (a) and post-test (b) EBSD maps of the mid-section of a pillar compressed at 25 °C, displaying transverse twins, as verified by a method in [10]; the EBSD colour scheme is the same as in Fig. 2. In (c) the DIC strain map of the same region is given, indicating that strain concentrates at the transverse twins. As reported previously, [10], deterioration of the Pt speckle pattern occurs above twinned regions, disrupting the DIC results, as arrowed in white. The black arrow indicates where transverse slip occurs.

Figure(s)

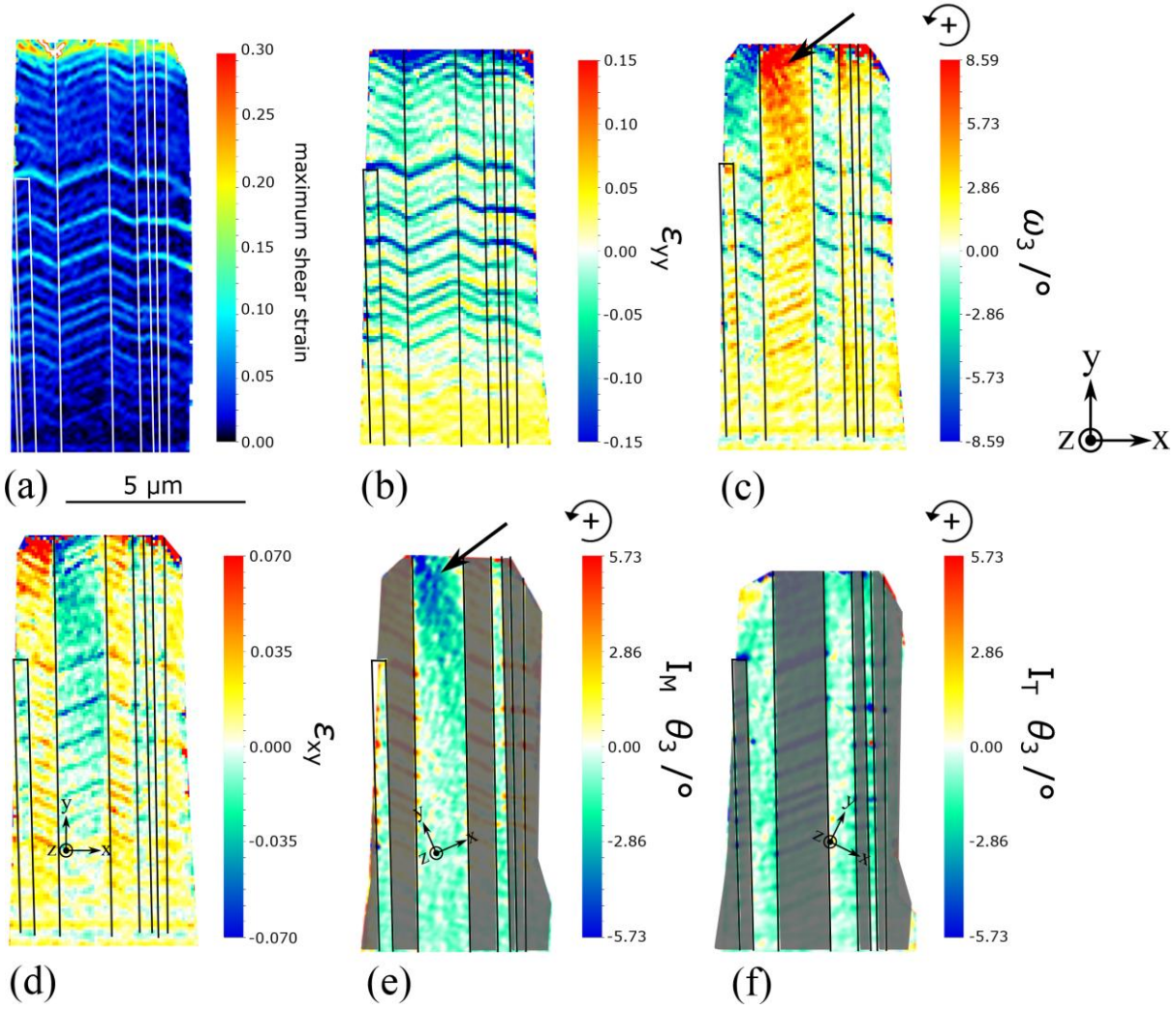

Figure 4 Further components of strain extracted from the DIC maps data in Fig. 2(e). ω_3 is the curl of the displacement field about the axis perpendicular to the surface of measurement; θ_3 describes the rotation of the underlying crystal lattice per γ-variant, and is extracted following a method outlined in [16].

Figure(s)

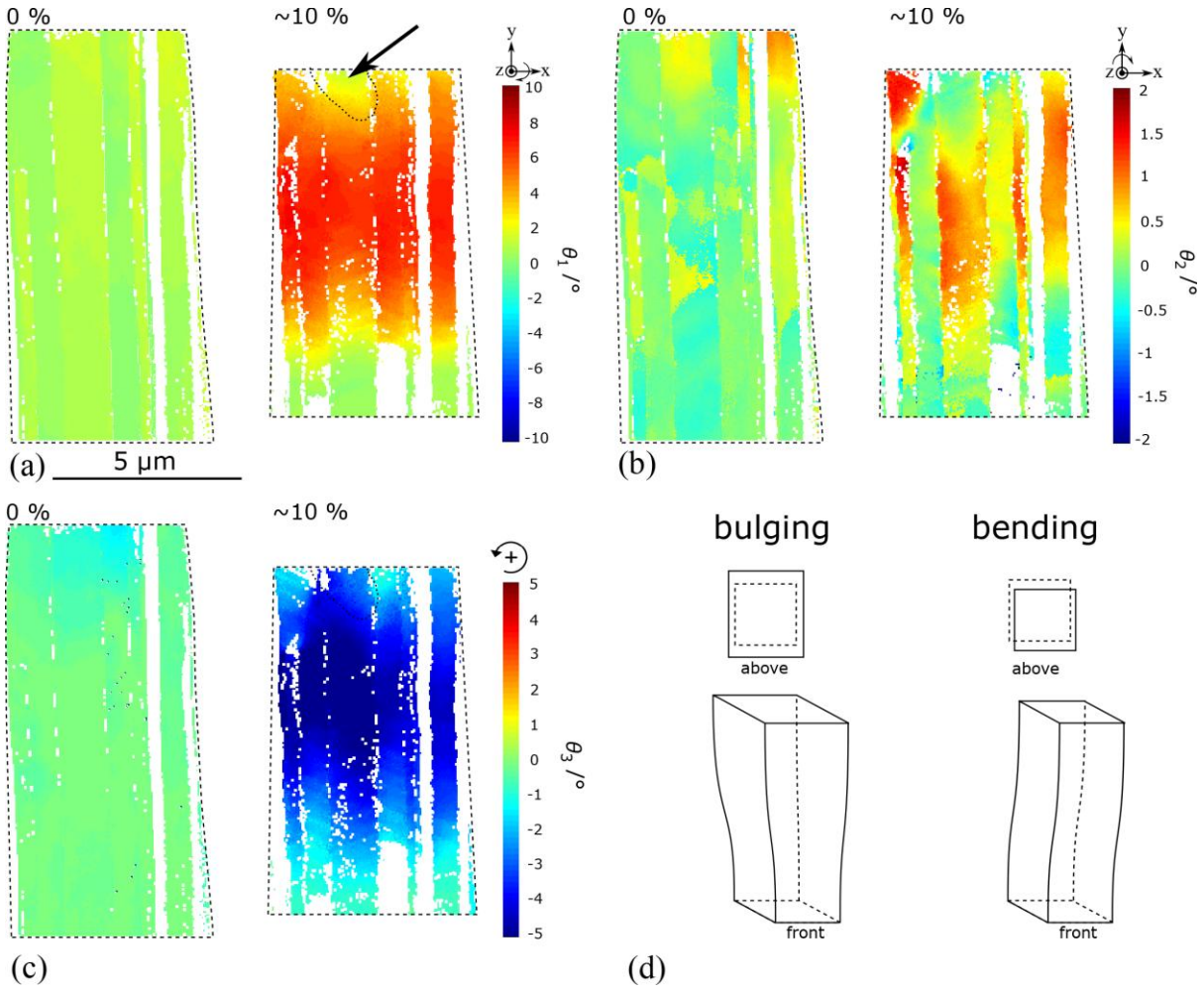

Figure 5 (a – c) rotation components θ_1, θ_2 and θ_3 of the γ-TiAl phase crystal lattice relative to the base of the pillar, extracted from the pre- and post-compression EBSD maps of the front face of the pillar compressed at 633 °C in Fig. 2. The effectiveness of the VarRe program is verified by application to the pre-compression state: all lamellae display θ_1, θ_2 and θ_3 values of zero, within the ~0.5° error of EBSD mapping. Note the different scales used for each rotation component. (d) schematic of the bulging and bending morphologies consistent with the crystal rotation of the front surface of the pillar.

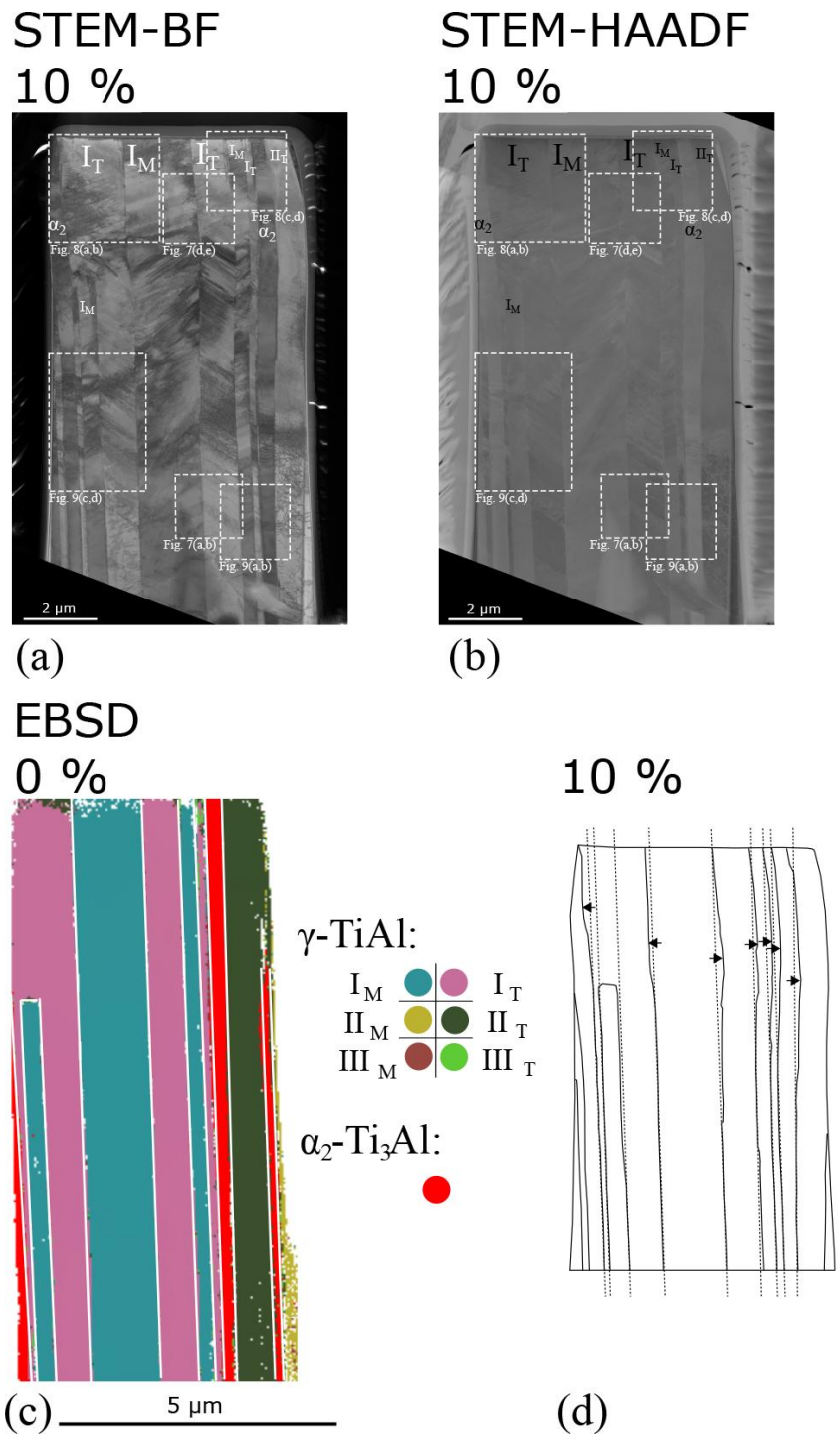

Figure 6 STEM BF (b) and HAADF (c) images of thin foil lift-out of the pillar compressed at 633 °C in Fig. 2, along with the pre-compression EBSD map of the pillar surface for comparison of the lamellar boundary structure into the pillar depth. (d) positions of the lamellar interfaces, extracted from (b), illustrating the lateral bulging of the upper region of the pillar; the dotted straight lines have been added as a guide to the eye. The STEM images were not taken normal to sample surface in order to increase the contrast on the deformation features; hence, lamellar boundaries appear to have a finite width in all the STEM images in the current work.

Figure(s)

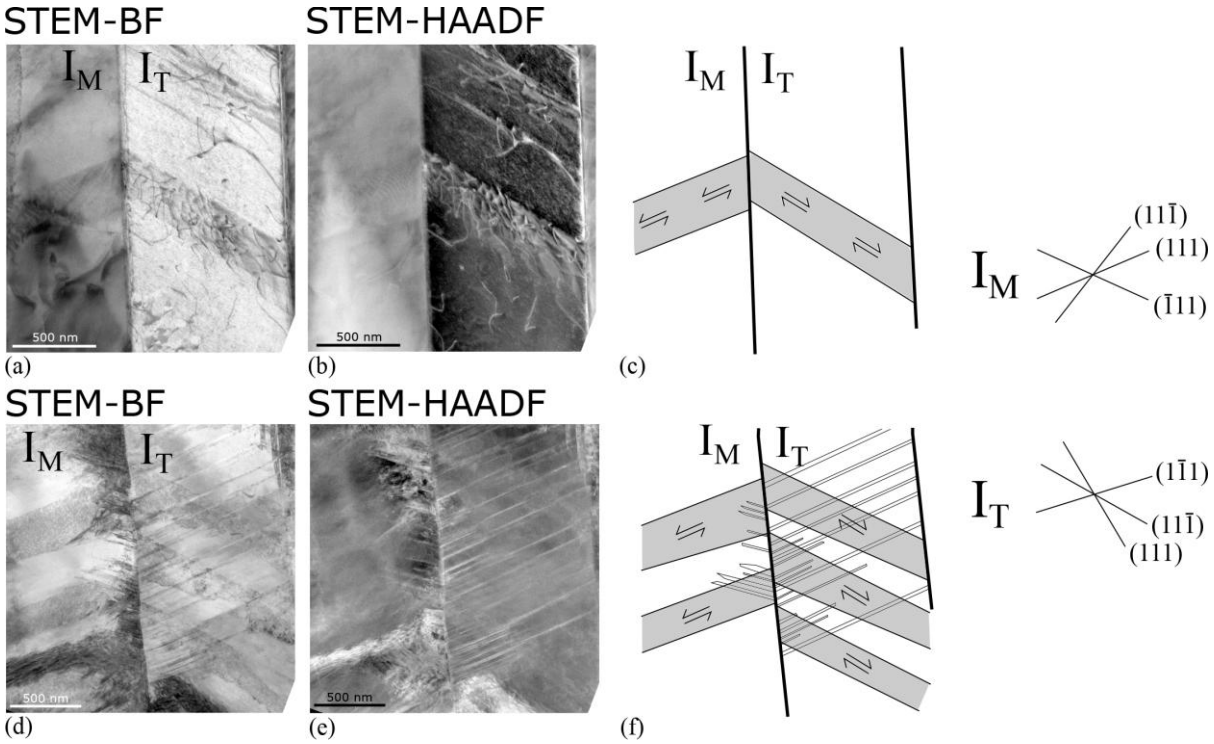

Figure 7 STEM BF (a,d) and HAADF (b,e) images of two regions indicated in Fig. 6 where plasticity occurs in mirror-symmetry coarse transverse bands in γ-TiAl lamellae. The drawings of the deformation structures (c,f) have been extracted from the STEM images; not all the fine nanotwins in (d,e) were reproduced in (f), for clarity.

Figure(s)

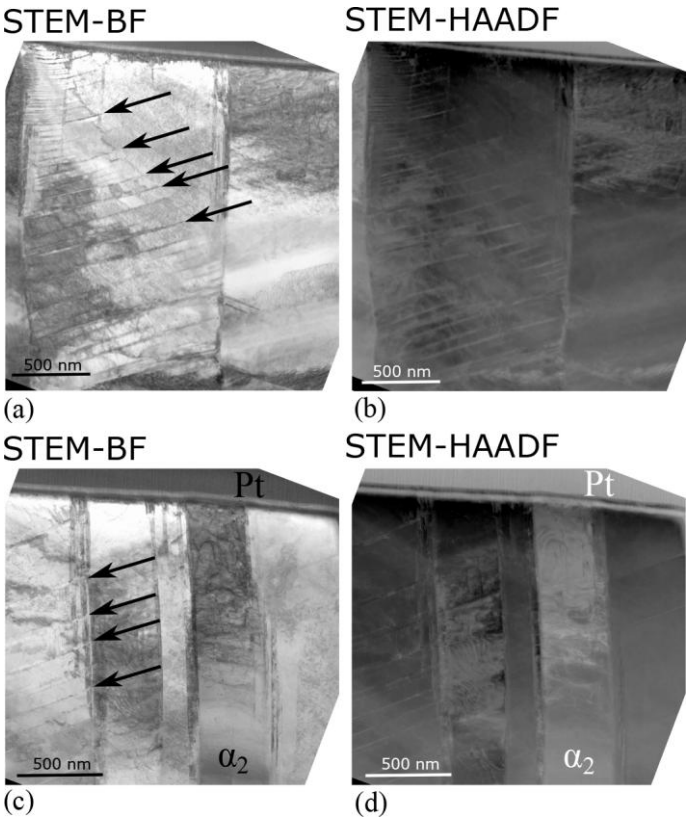

Figure 8 STEM BF (a,c) and HAADF (b,d) images of two regions at the top of the pillar, indicated in Fig. 6, where a dense array of fine twins, of which a few are arrowed in black, were observed to operate in γ-TiAl lamellae on the secondary twinning systems, and dislocation glide mediates plasticity in α_2 lamellae.

Figure(s)

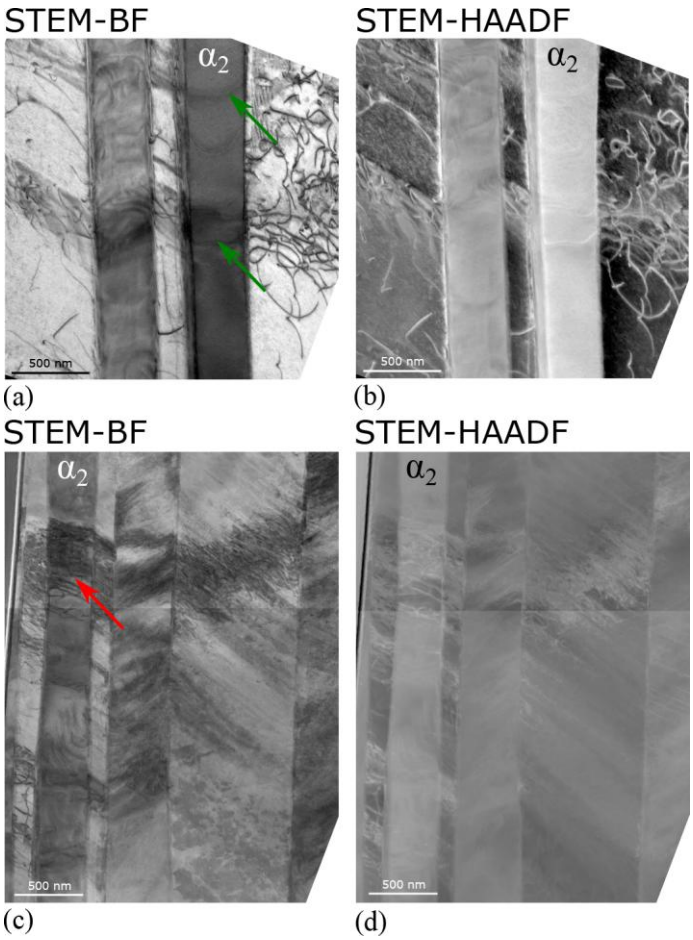

Figure 9 STEM BF (a,c) and HAADF (b,d) images of two regions from the mid-height of the pillar indicated in Fig. 6 where transmission of transverse strain across α_2 lamellae occurs in some cases by dislocation glide (arrowed in red). Green arrows indicate relatively dislocation-free propagation of transverse shear across an α_2 lamella.

Figure(s)

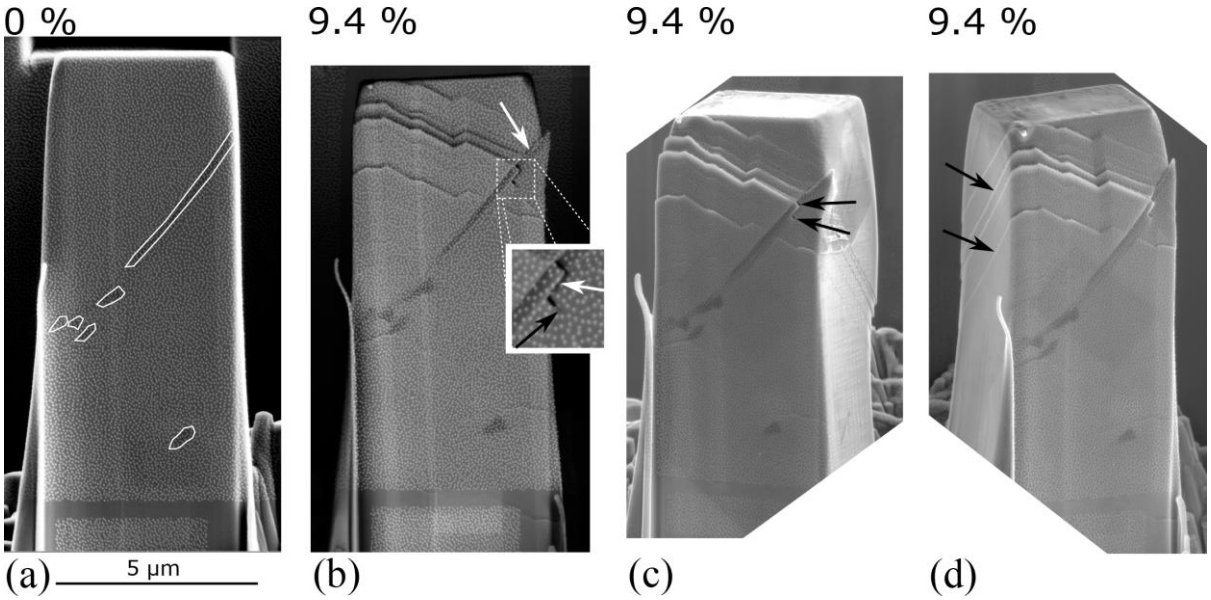

Figure 10 Secondary electron images before (a) and after (b – d) compression at 633 °C of a hard mode micropillar containing a TiB_2 flake, outlined in white in (a), that is seen to crack transversally and to debond from the γ-TiAl lamellar matrix; this resulted in a significantly lower yield stress for the onset of plasticity in Fig. 1(b) than in the absence of such boride particles. Transversal cracking of boride also extends into the γ-TiAl matrix, as arrowed in black in (b).

Figure(s)

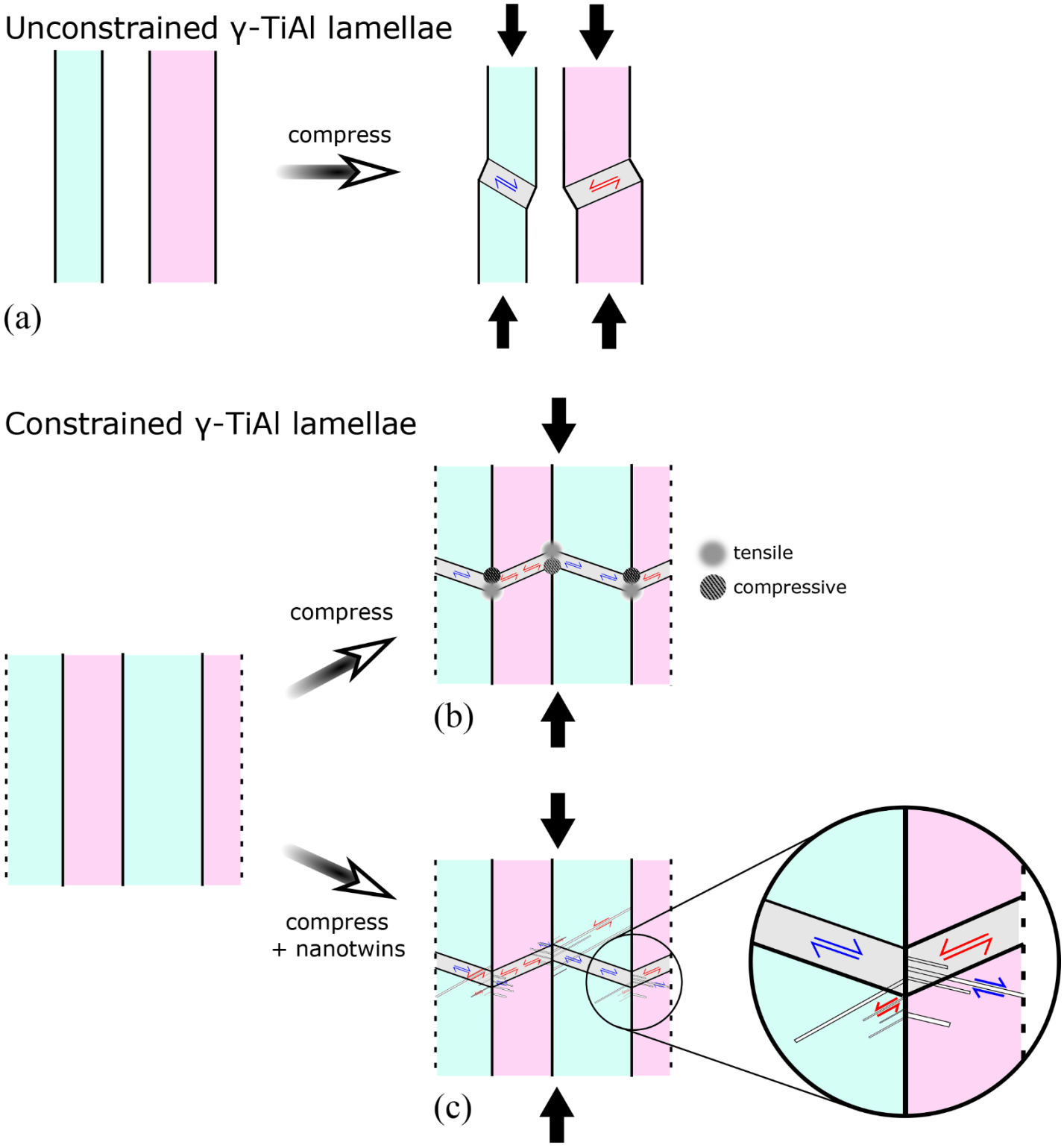

Figure 11 Schematic of the transverse twinning morphologies and strain accommodation mechanisms active upon mirror symmetry transverse twinning across true twin γ/γ interfaces.

Figure(s)

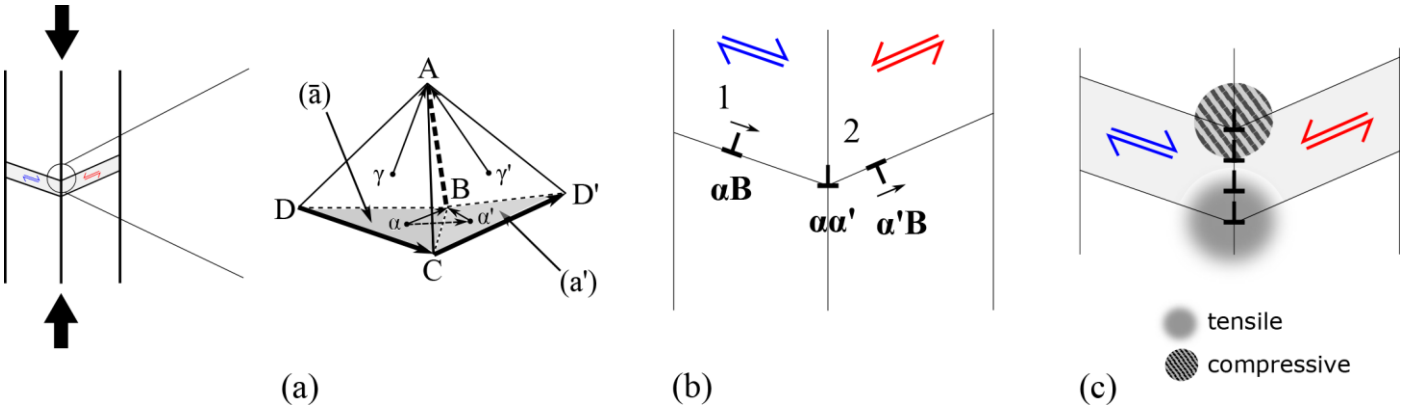

Figure 12 (a) double Thompson tetrahedron describing the $\{111\}_\gamma$ planes across a true twin γ/γ interface according to the original notation established in [25]. The bold lines indicate ordinary dislocation $<1\bar{1}0]$ directions; the rest of the tetrahadral edges are $<10\bar{1}]$ superdislocations. Greek letters indicate the centroids of triangular faces opposite the corresponding capital roman lettered vertice. The dislocation decomposition in (b) converts an incoming Shockley partial $<11\bar{2}]$ twinning dislocation into a twinning partial on the mirror-symmetry transverse twinning plane and leaves a residual low-angle tilt boundary edge dislocation at the lamellar interface, which results in the elastic stress gradient along the interface depicted in (c).

*Graphical Abstract

Microcompression at 633 °C

EBSD
0 %

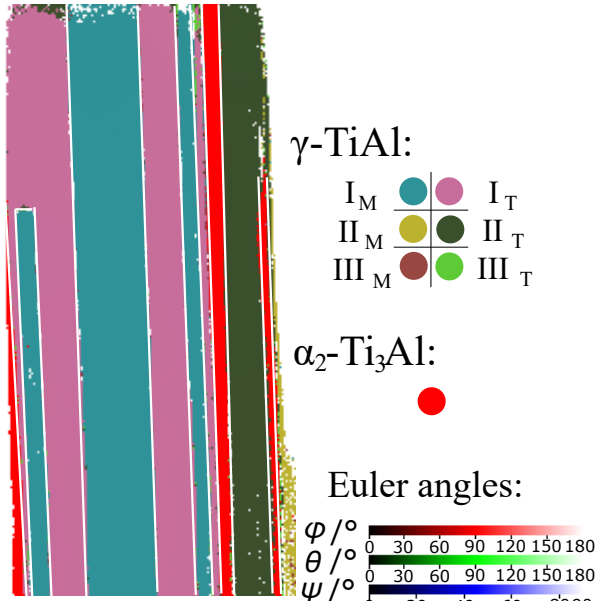

Digital Image Correlation
Strain Mapping

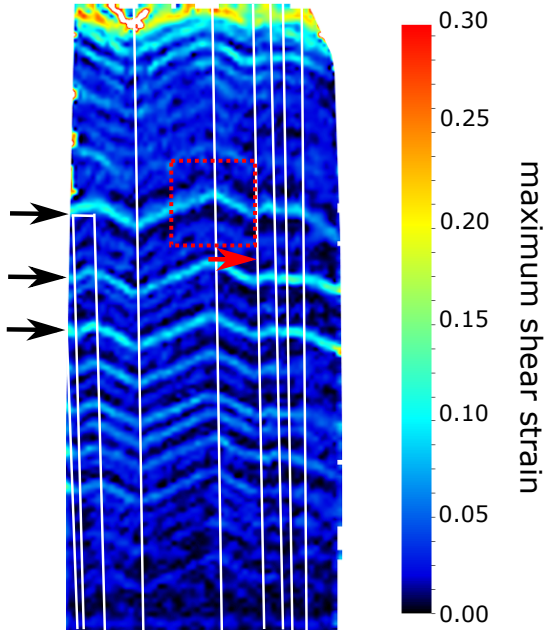

STEM-BF

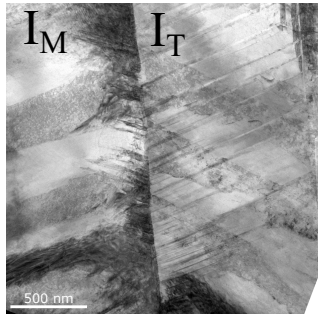

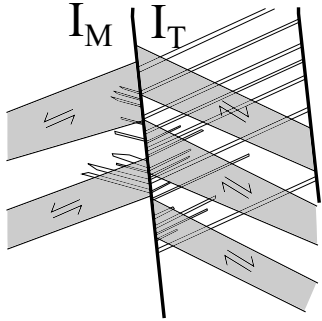

Schematic of Multi-scale Twinning